ADVANCED FUNCTIONAL MATERIALS
www.afm-journal.de

Light-Controlled Nanosystem with Size-Flexibility Improves Targeted Retention for Tumor Suppression

Huanhuan Luo, Li Kong, Feng Zhang, Chenglong Huang, Jiayi Chen, Hongbo Zhang, Han Yu, Song Zheng, Hongwei Xu, Yiran Zhang, Lianfu Deng, Gang Chen, Hélder A. Santos,* and Wenguo Cui**

Although great promise has been achieved with nanomedicines in cancer therapy, limitations are still encountered, such as short retention time in the tumor. Herein, a nanosystem that can modulate the particle size in situ by near-infrared (NIR) light is self-assembled by cross-linking the surface-modified poly(lactic-*co*-glycolic acid) from the up-conversion nanoparticle with indocyanine green and doxorubicin–nitrobenezene–polyethylene glycol (DOX–NB–PEG). The nanosystem with its small size (≈100 nm) achieves better tumor targeting, while the PEG on the surface of the nanosystem can effectively shield the adsorption of proteins during blood circulation, maintaining a stable nanostructure and achieving good tumor targeting. Moreover, the nanosystem at the tumor realizes the rapid shedding of PEG on its surface by NIR irradiation, and the enhanced cellular uptake. At the same time, aggregation occurs inside the nanosystem to form bigger particles (≈600 nm) in situ, prolonging the retention time at the tumor and producing enhanced targeted therapeutic effects. In vitro data show higher cellular uptake and a higher rate of apoptosis after irradiation, and the in vivo data prove that the nanosystem have a longer residence time at the tumor site after NIR irradiation. This nanosystem demonstrates an effective therapeutic strategy in targeted synergistic tumors.

1. Introduction

Nano-drug delivery system serves as an effective vehicle that can achieve targeted delivery of drugs to tumor sites.[1,2] As a result of the rapid growth of nascent endothelial cells in tumor cells, the interstitial space varies from 200 nm to 1.2 µm depending on the cell type.[3] Therefore, particles with a size of less than 200 nm are more likely to enter the interstitial space through the blood vessel wall, realizing targeted therapy and reducing the drug's side effects.[4–6] However, it has been reported that the size of the nanoparticles is negatively correlated with the cellular cytosol.[7] Thus, such particles with small size and good targeting are easier to be metabolized outside the body, reducing the retention time of the drug in the tumor site. While, the larger size is more likely to be retained in the tumor site.[8,9] Therefore, how to functionalize

H. Luo, Dr. C. Huang, J. Chen, H. Yu, S. Zheng, H. Xu, Prof. G. Chen
Jiaxing Key Laboratory of Basic Research and Clinical Translation on Orthopedic Biomaterials
Department of Orthopaedics
The Second Affiliated Hospital of Jiaxing University
1518 North Huancheng Road, Jiaxing 314000, P. R. China
E-mail: adcyy@aliyun.com

H. Luo, F. Zhang, Prof. H. Zhang, Dr. Y. Zhang, Prof. L. Deng, Prof. W. Cui
Department of Orthopaedics
Shanghai Key Laboratory for Prevention and Treatment of Bone and Joint Diseases
Shanghai Institute of Traumatology and Orthopaedics
Ruijin Hospital
Shanghai Jiao Tong University School of Medicine
197 Ruijin 2nd Road, Shanghai 200025, P. R. China
E-mail: wgcui80@hotmail.com

The ORCID identification number(s) for the author(s) of this article can be found under https://doi.org/10.1002/adfm.202101262.

DOI: 10.1002/adfm.202101262

Dr. L. Kong
Tongji School of Pharmacy
Huazhong University of Science and Technology
Wuhan 430030, P. R. China

F. Zhang, Prof. H. A. Santos
Drug Research Program
Division of Pharmaceutical Chemistry and Technology
Faculty of Pharmacy
University of Helsinki
Helsinki FI-00014, Finland
E-mail: helder.santos@helsinki.fi

Prof. H. Zhang
Pharmaceutical Sciences Laboratory and Turku Bioscience Center
Åbo Akademi University
Turku FI-20520, Finland

Prof. H. A. Santos
Helsinki Institute of Life Science (HiLIFE)
University of Helsinki
Helsinki FI-00014, Finland

the nanocarriers so that they can flexibly regulate the size of the nanoparticles, which can not only target the tumor site with a smaller particle size, but also increase the particle size in situ at the tumor site to extend the retention time, is a very crucial step needed to enhance the therapeutic antitumor effect.

The structure and function of the functionalized nanocarriers will be transformed when they are exposed to the stimuli from external factors.[10–13] Several polymers have introduced some relevant function into their structure, which may undergo changes, such as hydrolysis, fracture, or swelling in response to the environmental stimuli, further triggering the transformation of the nanostructure.[14] For instance, polymers based on the radicals of selenide, thioacetone, and borate will undergo a responsive phase transition and change their structural function upon reactive oxygen species (ROS) stimulation.[15–18] Disulfide-based polymers can react with high glutathione in the tumor microenvironment to form sulfhydryl groups.[19,20] Polymers based on hydrazone bonds,[21] hemiacetals,[22] vinyl ethers,[23] and other structures can break upon acid stimulation, resulting in rapid drug release. Moreover, light has been considered as a flexible, precise, and non-invasive element for "smart" therapy.[24–26] Majority of the light-responsive materials is sensitive to ultraviolet, such as azobenzenes,[27] nitrobenzenes,[28] spiropyrans,[29] and diarylenes.[30] However, limitations of transformation and application still remain, because of the poor tissue penetration. Therefore, it is essential to design such a light-controlled nanosystem that could regulate the structure changes in response to changes in the environment and overcome the difficulty of poor penetration.

It has been reported that up-conversion luminescent materials can emit light with high frequency after being excited by light with low energy.[28,31,32] In order to improve the penetration of the light, some up-conversion materials were introduced into the light-controlled nanosystem. As a result, we hypothesize that such nanosystem could convert the penetrating near-infrared (NIR) light into ultraviolet (UV) light in situ to stimulate the nanosystem. In addition, the photosensitizer in the nanosystem could also convert the light energy into heat or generate ROS to produce photothermal or photodynamic therapeutic effect.[33–38]

Herein, an NIR light-controlled nanosystem with size-flexibility in situ at the tumor site was successfully constructed by the cross-linking of poly(lactic-*co*-glycolic acid) (PLGA) with the UV-sensitive polymer doxorubicin–nitrobenezene–polyethylene glycol (DOX–NB–PEG) and indocyanine green (ICG), achieving a size regulation from 100 to 600 nm at the tumor site under 980 nm activation, which not only enhanced the tumor targeting and retention, but generated a synergistic therapy of phototherapy and chemotherapy for the osteosarcoma therapy (**Scheme 1**). After intravenously injected into the mice bearing MNNG/HOS tumor, the nanosystem with small size (≈100 nm) and inert surface maintained a stable structure and was delivered into the tumor site. Moreover, the optical time for the nanosystem to get into the tumor was captured by fluorescence imaging. Then, after exposed to the NIR irradiation (980 nm) at the optical time, the nanosystem in the osteosarcoma converts the NIR to UV light, stimulating responsive breakage of nitrobenzene on the polymer DOX–NB–PEG, stripping off the surface of PEG, inducing the changes of the surface of nanosystem from hydrophilic to hydrophobic, and promoting enhanced uptake of nanoparticles by the tumor cells. At the same time, responsive aggregation occurred within the nanosystem, resulting in larger-sized nanoparticles in situ. When the particles reach a certain size, their surface tension was balanced with the fluid tension in the microenvironment, and then they can be stabilized at a larger size that remained for enhanced retention time. Finally, the tumor was irradiated again with 785 nm irradiation in order to provide a synergistic simultaneous photothermal and photodynamic therapy.

2. Results and Discussion

UV-sensitive polymer DOX–NB–PEG was synthesized according to the synthetic route as described in Scheme S1, Supporting Information, and the chemical structure was determined using ^{1}H NMR (Figure S1, Supporting Information) and electrospray ionization mass spectrometry analysis (Figure S2, Supporting Information). In order to study the effect of UV on DOX–NB–PEG (**Figure 1**A), the absorption spectra (Figure 1B) and fluorescence emission spectra (Figure 1C) were evaluated. The results show that the chemical modification did not affect the structural stability of DOX. In addition, we investigated the reaction kinetics of the reaction using high performance liquid chromatography (HPLC). Figure 1D,E indicates that the content of DOX–NB–PEG changed negatively with the increasing of the UV irradiation time, and almost 90% of the polymer was decomposed at 10 min UV irradiation time, which further demonstrated the UV sensitivity of DOX–NB–PEG.

Then, a NIR light-controlled nanosystem (here designated as UIDOP micelles) with size-flexibility in situ at the tumor site was successfully constructed by cross-linking of PLGA from the surface of up-conversion nanoparticle (UCNP) with ICG and DOX–NB–PEG. UIDOP micelles had loading levels of 28.5% ICG and 6.3% DOX, and respective loading efficiencies of 87.1% and 95.6%. As observed under transmission electron microscope (TEM; **Figure 2**A,B), both UCNPs and the UIDOP micelles had a uniform morphology, showing the individual diameter of 21.9 ± 1.3 and 102.3 ± 4.6 nm. After the nanosystem was exposed to the NIR irradiation (980 nm), it aggregated to form particles with a size of 601.9 ± 11.1 nm (Figure 2C), which greatly improved the retention of drug at the tumor site. Dynamic light scattering also indicates that the size of the UIDOP micelles increased from 104.1 to 603.7 nm after exposure to the NIR irradiation (980 nm) (Figure 2D). These nanosystems with a controlled particle size play a great important role in tumor targeting and retention. Moreover, the UIDOP micelles resulted in a good chemical stability in different media (Figure 2E) and they also possess an enhanced absorbance under irradiation (785 nm) as compared to free ICG (Figure S4, Supporting Information), which is a better characteristic for the photodynamic and photothermal therapy.

Next, the photoconversion ability of the UIDOP micelles was evaluated. We first confirmed the photoconversion of the nanosystem to singlet oxygen under irradiation using 1,3-diphenylisobenzofuran (DPBF) as a probe.[39] The absorption of the DPBF mixed with UIDOP micelles at 415 nm were measured during 600 s irradiation. This showed that UIDOP micelles produced more singlet oxygen after 600 s irradiation

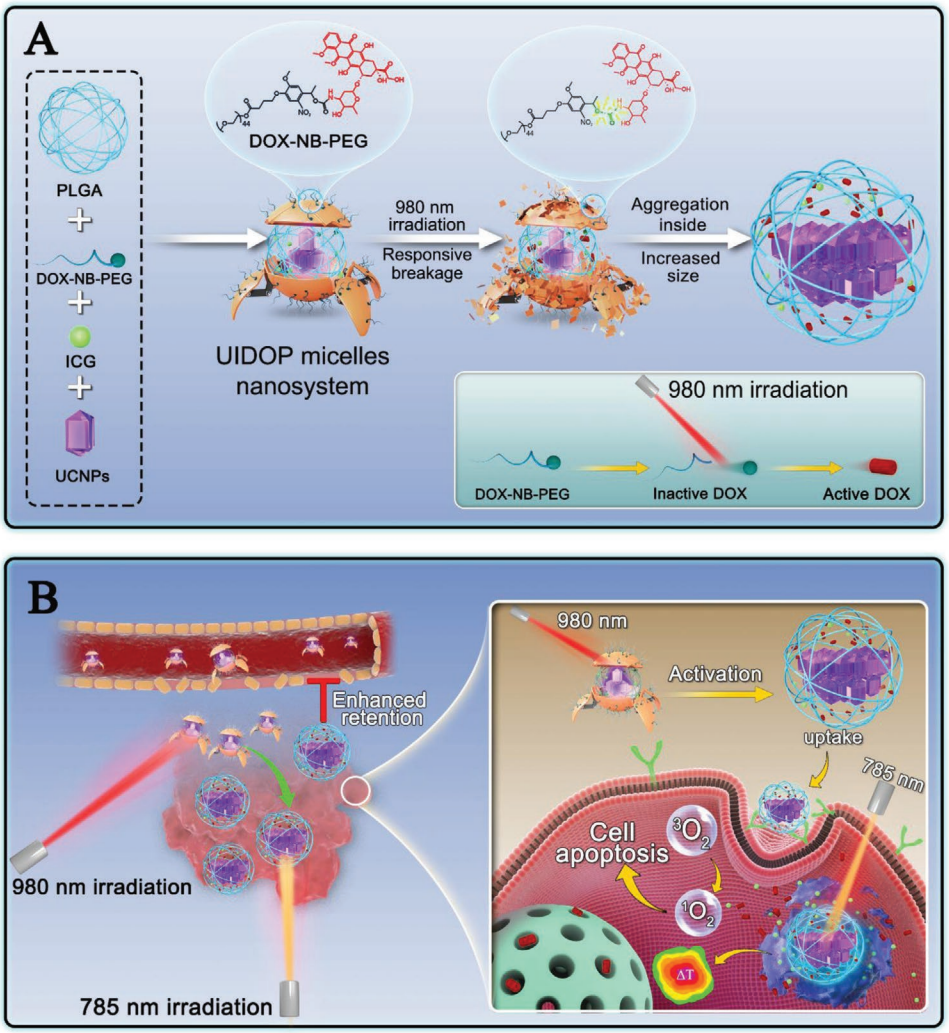

Scheme 1. Schematic illustration of nanosystem assembly, size-flexibility, and tumor therapy. A) The self-assembly of the nanosystem UIDOP micelles and the regulation of the size. B) The synergistic therapy mechanism.

as compared to free ICG (Figure 2F). Then, we further assessed the ability of the nanosystem to generate photothermal effects under irradiation. The temperature of the solution was investigated every 30 s during the whole irradiation and the cooling process. Free ICG and UIDOP micelles under 785 nm irradiation exhibited the photothermal conversion efficiencies (η) of 15.49% and 18.22% (Figures S5A and S5B, Supporting Information), respectively. By contrast, UIDOP micelles activated by 980 nm irradiation first and then under 785 nm irradiation were found to have the photothermal conversion efficiencies of 25.35% (Figure 2G), which was much higher than those used at 785 nm irradiation only. The UIDOP micelles with activated by 980 nm irradiation were in higher aggregation, which may cause favorable non-radiative transition under 785 nm irradiation. In addition, we also monitored the temperature elevation of the UIDOP micelles after activation with 980 nm irradiation at different concentration values, using a thermal imager. A concentration-dependent temperature elevation at 785 nm irradiation was also observed (Figure 2H).

To assess the ability of the UIDOP micelles to enhance the cellular uptake of the tumor cells, we studied their internalization by MNNG/HOS osteosarcoma cells (**Figure 3**A). The amount of ICG in cells was detected after the incubation of the UIDOP micelles and free ICG with MNNG/HOS cells for 6 and 24 h, respectively. UIDOP micelles showed preferable internalization after 6 and 24 h-incubation as compared to free ICG, indicating a promising capacity of their nanostructure to improve the cellular uptake. Moreover, the UIDOP micelles activated at 980 nm irradiation resulted in a more significant internalization by MNNG/HOS cells. The explanation for this is that the UIDOP micelles underwent responsive breakage of nitrobenzene on the polymer DOX–NB–PEG after 980 nm irradiation, stripping off the inert surface PEG and promoting the cellular uptake of the nanosystem.

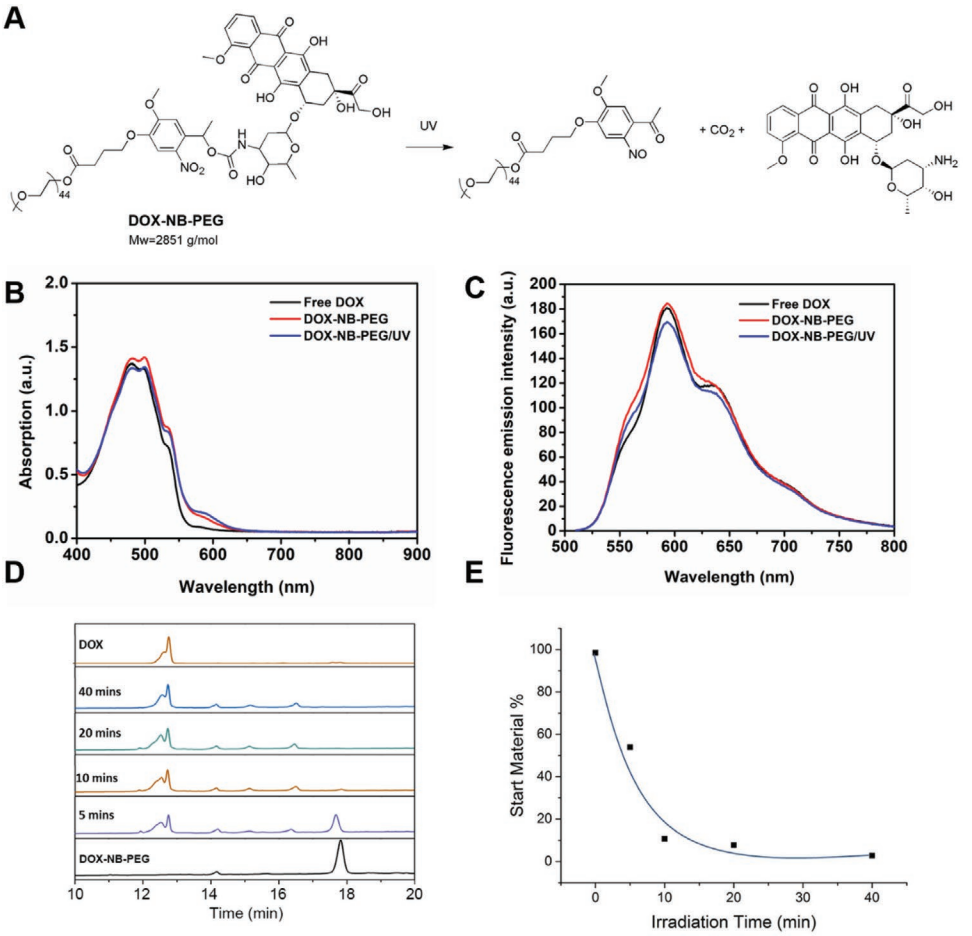

Figure 1. Characterization of the polymer DOX–NB–PEG. A) The decomposition route of DOX–NB–PEG. B) The absorption spectra and C) the fluorescence emission spectra of free DOX, DOX–NB–PEG, and DOX–NB–PEG/UV. D) The chromatogram of DOX and DOX–NB–PEG under UV irradiation at different times. E) The reaction kinetics of DOX–NB–PEG under UV irradiation.

To investigate the cell damage, we evaluated the cell viability of the nanosystem UIDOP micelles and their control groups under irradiation or without. Compared with free DOX, DOX–NB–PEG reduced the cell damage and improved the safety as a result of the inert surface of PEG (Figure S6A,B, Supporting Information). When the concentration of UCNP contained in the nanosystem was below 20 μg mL^{-1}, there was no toxicity (Figure 3B). After activated with 980 nm irradiation, UCNP also induced cell damage (Figure 3B,C). Furthermore, UCNP@DOX-NB-PEG activated with 980 nm irradiation exhibited a cytotoxicity of 7.05 μg mL^{-1} IC_{50} due to chemotherapy alone (Figure 3D). ICG-M had an IC_{50} value of 14.23 μg mL^{-1} under 785 nm irradiation as a result of the phototherapy alone (Figure 3E). In contrast, UIDOP micelles activated with 980 nm irradiation induced a distinct cytotoxicity of 4.17 μg mL^{-1} by both chemotherapy and phototherapy (Figure 3F). In order to further study the synergistic therapy of the UIDOP micelles, the combination index (CI) was calculated. The CI of UIDOP micelles was 0.88, indicating an effective synergistic therapy.

To further demonstrate the cell damage of the UIDOP micelles, we first employed calcein acetoxymethyl ester (Calcein-AM) and propidium iodide (PI) to detect the cellular state.[40] Figure 3G shows that UIDOP micelles activated with 980 nm irradiation exhibited higher rate of dead cells after 785 nm irradiation for 3 min. Afterward, we also studied the apoptosis of the MNNG/HOS cells treated with these groups using Annexin/PI staining by flow cytometer. UIDOP micelles activated with 980 nm irradiation resulted in 31.9% and 20.2% of the early and late apoptosis after 785 nm irradiation, respectively, much higher than that of ICG-M or DOX–NB–PEG alone (Figure 3H).

To confirm the generation of singlet oxygen in vitro, dihydroethidium (DHE) was used to detect it. MNNG/HOS cells were treated with UIDOP micelles activated with 980 nm irradiation or without for 6 h, and incubated with DHE for 30 min after irradiation with 785 nm for 3 min or without at once. Red fluorescence was observed in the UIDOP micelles with the irradiation, indicating the generation of singlet oxygen (Figure S7, Supporting Information). It has been reported that the presence of singlet oxygen induces the rupture of the lysosome, so we further observed the MNNG/HOS cells using acridine orange staining. UIDOP micelles under 980 nm and 785 nm irradiation only showed green fluorescence that is significantly different from that without irradiation, which indicates the lysosomal rupture of the cells (Figure S8, Supporting Information).

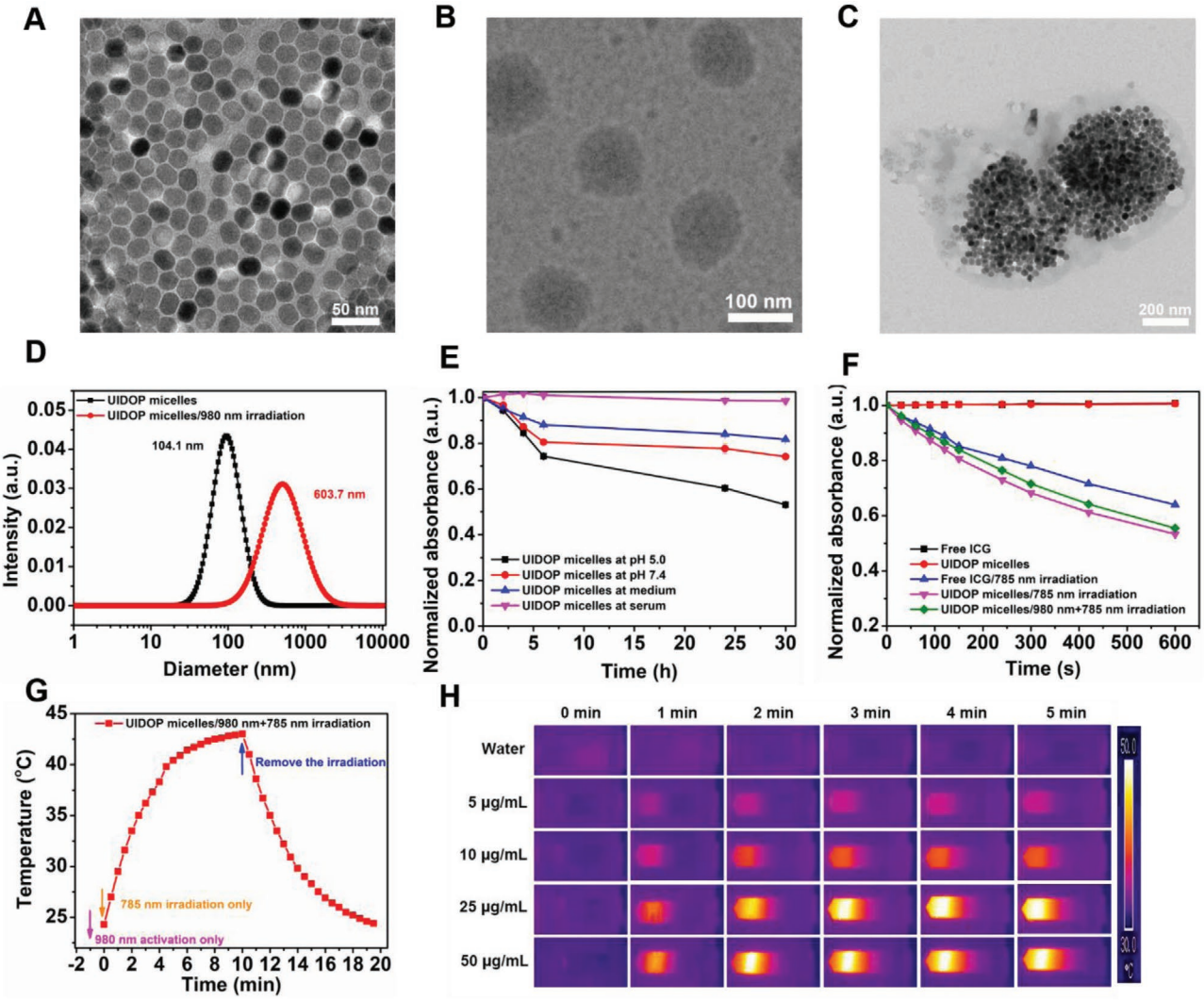

Figure 2. Preparation and characterization of the nanosystem UIDOP micelles. A) TEM image of UCNPs. B) TEM image of UIDOP micelles. C) TEM image of UIDOP micelles activated by 980 nm irradiation. D) Size distribution of UIDOP micelles under 980 nm activation or without. E) Chemical stability of UIDOP micelles (n = 3). F) Normalized absorbance of DPBF at 415 nm. G) Photothermal conversion efficacy of UIDOP micelles under 980 nm activation and 785 nm irradiation. H) Photothermal effect of UIDOP micelles under 980 nm activation and 785 nm irradiation at different concentration values.

Subsequently, in order to further explore the intracellular distribution of the nanosystem, LysoTracker green DND 26 (green) and Hoechst 33342 (blue) were employed to observe the cellular substructure of lysosome and nucleus (**Figure 4**A). MNNG/HOS cells were treated with the UIDOP micelles activated with 980 nm irradiation or without for 2 h, followed by the incubation with Hoechst 33342 for 10 min and LysoTracker green DND 26 for 5 min. UIDOP micelles with red fluorescence displayed a colocalization with lysosome. However, UIDOP micelles activated with 980 nm irradiation exhibited a brighter fluorescence and better colocalization (86.7%) with lysosome, indicating an enhanced cellular uptake. The lysosomes of MNNG/HOS cells treated with activated UIDOP micelles were ruptured after irradiation with 785 nm for 3 min and the colocalization decreased to 67.7%, promoting the cytoplasmic transportation.

In order to explore the ability of the UIDOP micelles to inhibit the growth of blood vessel, we used HUVEC cells for cellular tubulation studies (Figure 4B). The HUVEC cells treated with PBS, cancer media collected after incubated with MNNG/HOS cells, and UIDOP micelles were able to form tubes, but the cells treated with activated UIDOP micelles did not show the ability of cellular tubulation after irradiation with 785 nm. According to the analysis by image J, the number of junctions, meshes, and length significantly decreased (Figure 4C–E). Thus, UIDOP micelles activated with 980 nm irradiation possess the capacity to inhibit the growth of blood vessel, making the tumor cells starving from nutrition.

To further demonstrate the retention ability of the UIDOP micelles, we first investigated the mice bearing MNNG/HOS tumor cells treated with UIDOP micelles using NIR-Fluorescence (NIRF) imaging. The mice treated with the UIDOP micelles showed increased fluorescent signals as compared to free ICG/DOX (**Figure 5**A,B), indicating that the nanosystem with small size possesses excellent ability of tumor targeting. Moreover,

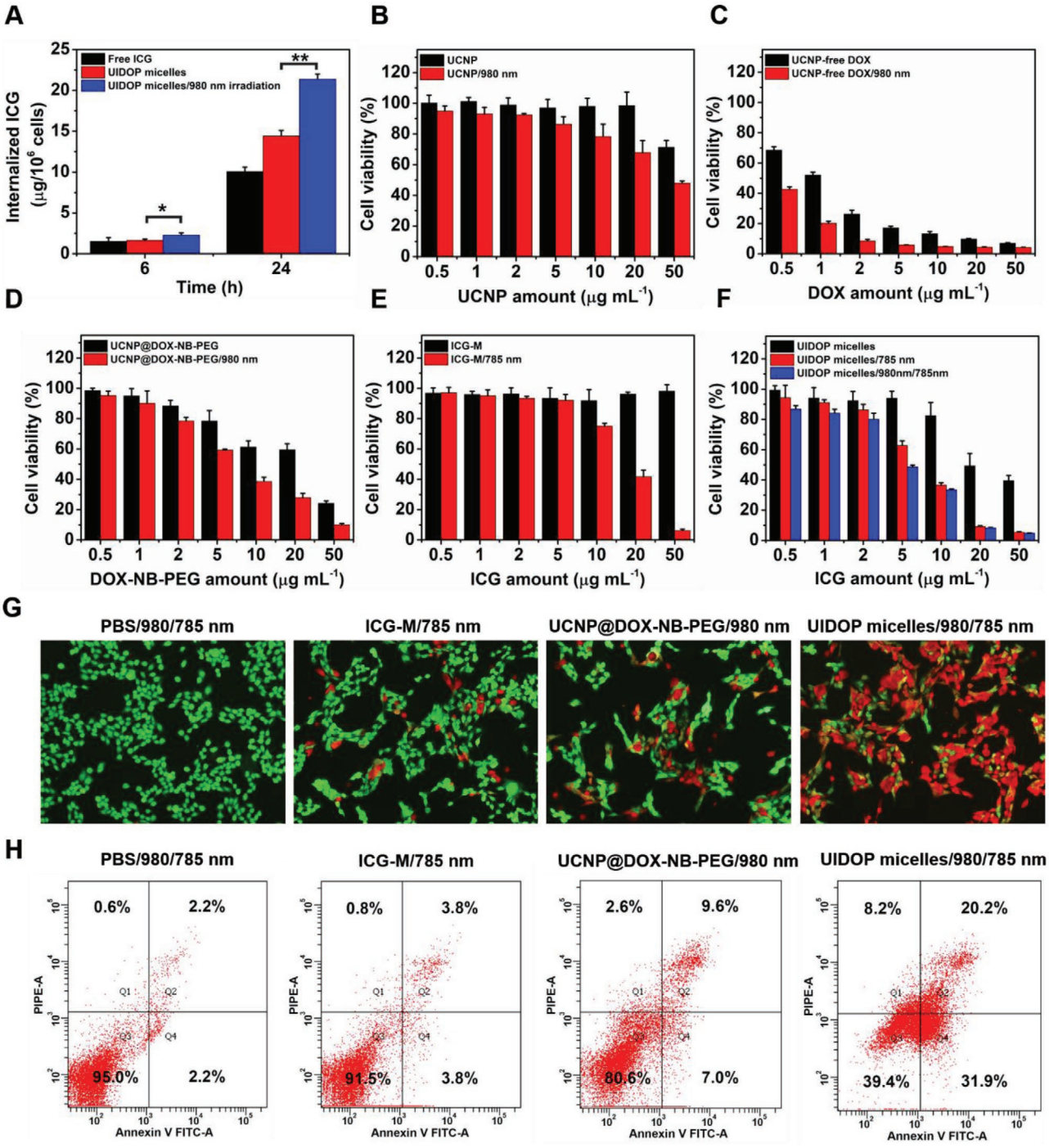

Figure 3. Endocytosis, cytotoxicity, and apoptosis studies. A) Internalized amount of ICG in MNNG/HOS cells treated by free ICG, nanosystem UIDOP micelles, and activated nanosystem UIDOP micelles by 980 nm irradiation after 6 and 24 h-incubation ($n = 3$, $P_{(6h)} = 0.0493$, $P_{(24h)} = 0.00277$). B–F) Cell viability of different samples ($n = 4$). G) MNNG/HOS cells stained by calcein-AM (green) and PI (red) after 6 h-incubation with PBS, ICG-M, UCNP@DOX–NB–PEG, and UIDOP micelles under 980 or 785 nm irradiation. H) Cell apoptosis level of MNNG/HOS cells stained by Annexin V FITC/PI after 24 h-incubation with PBS, ICG-M, UCNP@DOX–NB–PEG, and UIDOP micelles under 980 or 785 nm irradiation.

the nanosystem also showed better retention in tumor after activated with 980 nm irradiation than without it. Afterward, the biodistribution of the nanosystems activated with 980 nm irradiation or without was also examined at 24 and 72 h post-injection (Figure 5C–E). It was observed that the activated nanosystem with larger size possesses better ability for tumor retention.

Furthermore, we employed an infrared thermography to monitor the photothermal effect in vivo. The mice bearing MNNG/HOS tumor cells were intravenously injected with free ICG and the UIDOP micelles at the doses of 5.0, 7.5, and 10.0 mg kg^{-1}, followed by the activation with 980 nm irradiation or without at 24 h post-injection. Then the infrared thermography was performed

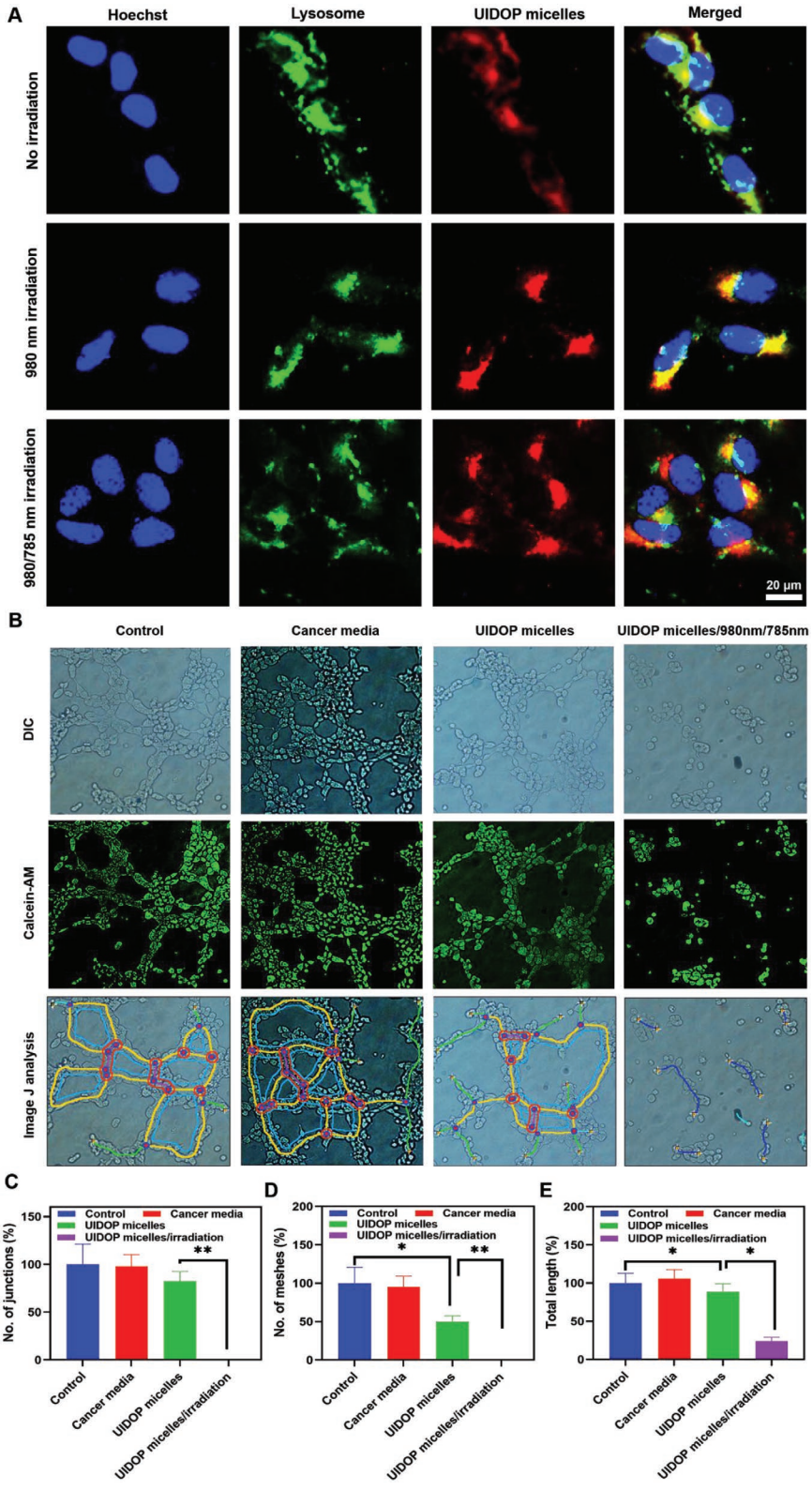

Figure 4. Intracellular studies and vessel inhibition analysis. A) MNNG/HOS cells stained by Hoechst 33342 and LysoTracker green DND 26 after 2 h-incubation with UIDOP micelles under 980 nm activation and 785 nm irradiation or without. B) HUVEC cells stained with calcein-AM after incubation with PBS, cancer media, UIDOP micelles, and UIDOP micelles under 980 nm activation and 785 nm irradiation ($n = 3$). C) Image J analysis of junctions ($P = 0.00506$). D) Image J analysis of meshes ($P_{(\text{UIDOP micelles:control})} = 0.0315$, $P_{(\text{UIDOP micelles/irradiation:UIDOP micelles})} = 0.00816$). E) Image J analysis of total length ($P_{(\text{UIDOP micelles:control})} = 0.0493$, $P_{(\text{UIDOP micelles/irradiation:UIDOP micelles})} = 0.0126$).

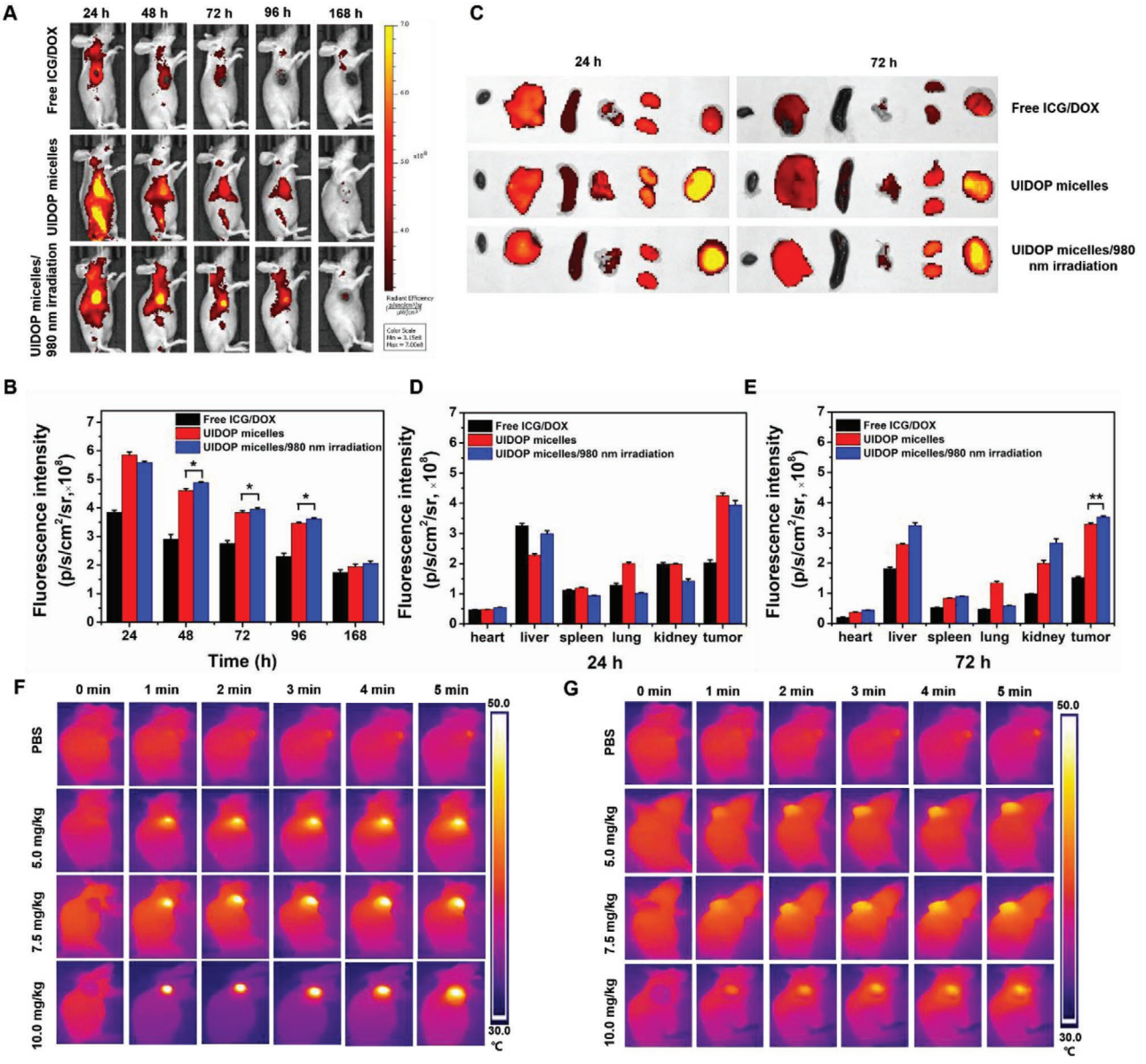

Figure 5. Tumor targeting, retention, and infrared thermography studies. A) In vivo NIRF images and B) their fluorescence intensity of different group ($n = 3$, $P_{(48h)} = 0.0229$, $P_{(72h)} = 0.0368$, $P_{(96h)} = 0.0478$). C) Ex vivo biodistribution and their fluorescence intensity at D) 24 h and E) 72 h of free ICG/DOX, and UIDOP micelles under 980 irradiation or not ($n = 3$, $P_{(tumor)} = 0.001397$). F) Infrared thermography images of UIDOP micelles under 980 nm activation and 785 nm irradiation. G) Infrared thermography images of free ICG/DOX under 785 nm irradiation.

with 785 nm irradiation. The UIDOP micelles activated with 980 nm irradiation exhibited a dose-dependent temperature elevation in the tumor from the mice bearing MNNG/HOS tumor cells with 785 nm irradiation (Figure 5F and Figure S9A, Supporting Information). In contrast, the free ICG/DOX showed no statistically significant differences in the temperature elevation, indicating the important role here of designed nanostructure (Figure 5G and Figure S9B, Supporting Information).

To verify the enhanced tumor suppression of the UIDOP micelles, we monitored the volume of the tumor in the mice bearing MNNG/HOS cells during 27 days (**Figure 6**A,B). The control group (PBS) with 980 and 785 nm irradiation resulted in 21-fold increase of the tumor volume, higher than the other groups tested. Free ICG/DOX showed approximately eightfold increase in the tumor volume in the absence or in the presence of 785 nm irradiation, indicating that the low temperature rise caused by the irradiation had no influence in the tumor growth. ICG-M exhibited good photothermal damage on the tumors with 785 nm irradiation. Complete tumor ablation occurred in four tumors at 15–19 days post-injection, but tumor recurrence occurred in three of these mice, which showed that photothermal therapy was still needed. UCNP@DOX–NB–PEG caused a twofold increase of tumor volume with 980 nm irradiation due to chemotherapy of DOX. Moreover, the UIDOP micelles activated with 980 nm irradiation at 24 h post-injection resulted in tumor ablation in all mice after 785 nm irradiation

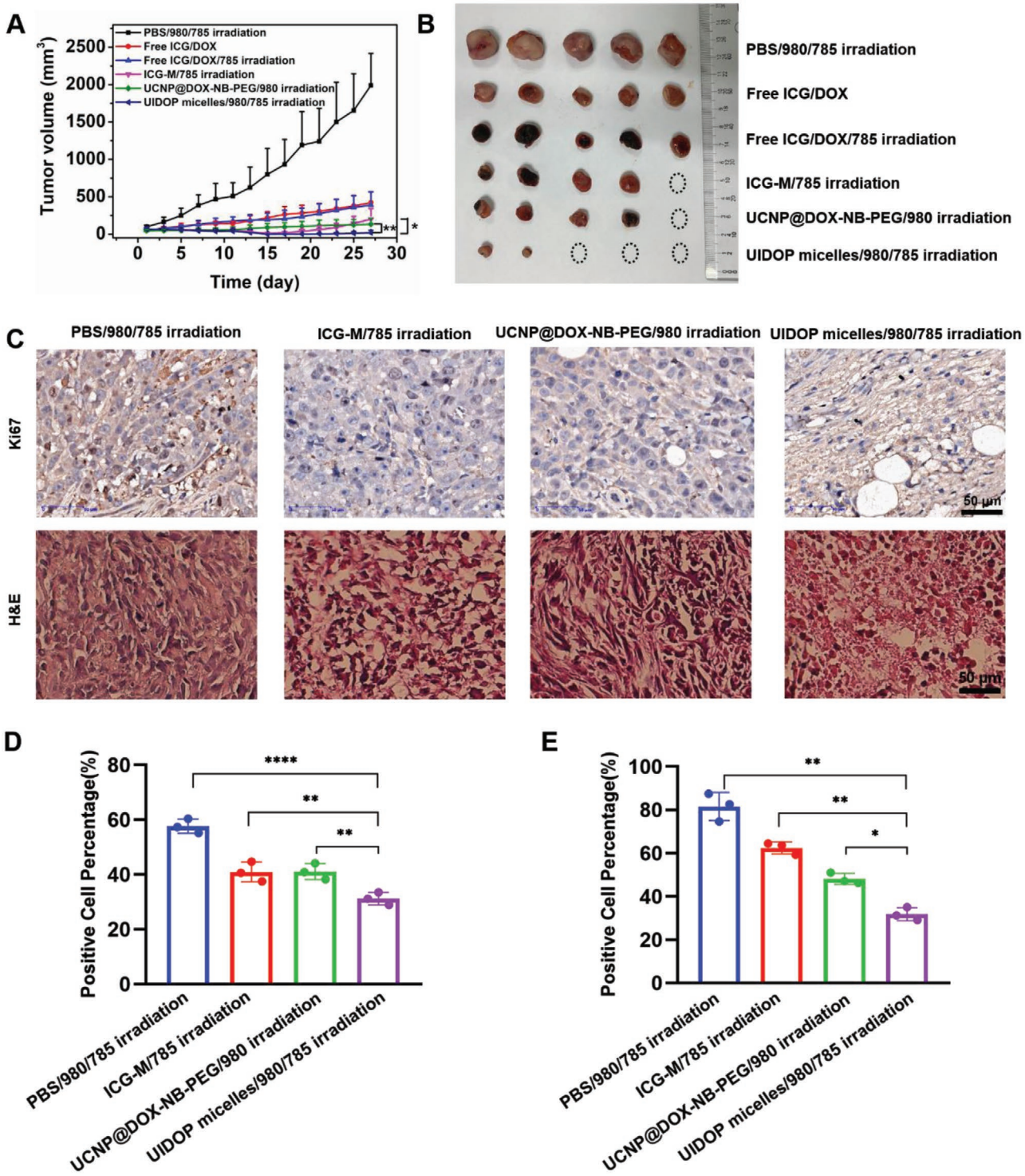

Figure 6. Synergistic therapy effect of the nanosystem UIDOP micelles. A) Tumor volume of different groups during 27 days ($n = 5$, $P_{(\text{UCNP@DOX–NB–PEG/980 irradiation:UIDOP micelles/980/785 irradiation})} = 0.0016$, $P_{(\text{ICG-M/785 irradiation:UIDOP micelles/980/785 irradiation})} = 0.018$). B) Photograph of tumors extracted from the mice at 27 days post-injection. C) Ki67 and H&E staining of the tumors ($n = 3$). D) Image J analysis of ki67 ($P_{(\text{PBS/980/785 irradiation:UIDOP micelles/980/785 irradiation})} = 0.0000667$, $P_{(\text{ICG-M/785 irradiation:UIDOP micelles/980/785 irradiation})} = 0.00626$, $P_{(\text{UCNP@DOX–NB–PEG/980 irradiation:UIDOP micelles/980/785 irradiation})} = 0.00144$). E) Image J analysis of H&E staining ($P_{(\text{PBS/980/785 irradiation:UIDOP micelles/980/785 irradiation})} = 0.00434$, $P_{(\text{ICG-M/785 irradiation:UIDOP micelles/980/785 irradiation})} = 0.00205$, $P_{(\text{UCNP@DOX–NB–PEG/980 irradiation:UIDOP micelles/980/785 irradiation})} = 0.0339$).

for 3 min, and there were two mice that had the tumor recurrence; the growth rate after recurrence was also reduced, which indicated the enhanced tumor suppression of the nanosystem.

Finally, we performed immunohistochemistry to further examine the tumor-damage ability (Figure 6C) and we used image J to analyze the photograph. Both the expression of ki67

and haematoxylin and eosin (H&E) stain showed severe cell damage at the tumor site from the mice treated with the activated UIDOP micelles under 785 nm irradiation (Figure 6D,E). In addition, they had no remarkable damage in normal tissues, such as heart, liver, spleen, lung, and kidney (Figure S10, Supporting Information). Thus, the UIDOP micelles are promising for their enhanced tumor suppression efficacy and safety.

3. Conclusion

In summary, we have established a NIR light-controlled UIDOP micelles with size-flexibility in situ tumor by cross-linking of PLGA from the surface of UCNP with ICG and DOX–NB–PEG. The UIDOP micelles exhibited high chemical stability and size-controlled nanostructure. Under 980 nm irradiation, the UIDOP micelles, which has been targeted to the tumor site with a smaller particle size, can spontaneously remove the surface of PEG at the tumor site and aggregate to form larger nanoparticles, prolonging their retention time in the tumor site and enhancing the chemotherapy effect. Furthermore, the designed UIDOP micelles not only generated photothermal and photodynamic therapy, but also inhibited the growth of tumor blood vessels, achieving a synergistic therapeutic effect. In vitro cellular experiments showed that the activated nanosystem enhanced the cellular uptake, cytotoxicity, and inhibited the blood vessel growth. Finally, the animal experiments further demonstrated the targeting and retention of activated nanosystem at the tumor site and their safety in normal tissues. Overall, the versatile design of light-controlled nanosystem with size-flexibility in situ possesses great potential in cancer therapy, though such type of nanosystem still requires further evaluation before clinical translation.

4. Experimental Section

Synthesis of Doxorubicin–Nitrobenezene–Polyethylene Glycol: Briefly, nitrobenezene–polyethylene glycol (NB–PEG) was synthesized by conjugation of PEG2000 and 4-(4-acetyl-2-methoxy-5-nitrophenoxy) butanoic acid first. To a stirred solution of NB–PEG (1.0 eq.) and 4-nitrophenyl chloroformate (3.0 eq.) in CH_2Cl_2, triethylamine (6.0 eq.) was added. The reaction mixture was stirred at room temperature in the dark overnight. Following solvent removal in vacuo, nitrophenyl–NB–PEG was used in the next step without further purification. To synthesize DOX–NB–PEG, nitrophenyl–NB–PEG (1.0 eq.) and doxorubicin hydrochloride (1.5 eq.) was dissolved in dimethylformamide (DMF). Then, solution was added with triethylamine (5.0 eq.) and stirred at room temperature in the dark overnight. CH_2Cl_2 was added into the reaction solution and washed with brine. The organic fraction was combined and solvent was removed under vacuo. Column chromatography (Gradient: CH_2Cl_2 to 2% of MeOH in CH_2Cl_2 to 10% of MeOH in CH_2Cl_2) was applied to purify the DOX–NB–PEG, yielding DOX–NB–PEG (60%) as a red powder (Scheme S1, Supporting Information).

Synthesis of the Light-Controlled Nanosystem: UCNP was purchased from Hangzhou Fluo Nanotech Co., Ltd. Briefly, 0.5 mg of UCNP and 0.5 mg of PLGA were mixed in 200 µL DMF. Next, 1 mg of ICG and 1 mg of DOX–NB–PEG were dissolved in 400 µL of DMF. Then, the above two solutions were mixed under ultrasonication. Subsequently, the mixture was dispersed into 4.5 mL of distilled water for 5 min under ultrasonication, followed by the dialysis for 24 h.

Characterization: NMR spectra (^{1}H) were measured on a Bruker AV-400MHz spectrometer. Chemical shifts were recorded in ppm. Tetramethylsilane (TMS) was used as an internal standard. Coupling constants are given in Hz. Matrix-assisted Laser desorption/ionization time of flight mass spectrometry (MALDI-TOF mass spectra) was acquired using an Applied Biosystems Voyager System 6069 MALDI-TOF mass spectrometer. α-Cyano-4-hydroxycinnamic acid was used as matrix in all cases. The morphology was characterized using TEM imaging (Hitachi H-600). The size distribution was measured by Zetasizer Nano ZS90 (Malvern). The absorption spectra were characterized using a microplate reader (Multiskan GO). The fluorescence emission spectra were detected by fluorescence spectrophotometer (LS 55, PerkinElmer). The temperature of the samples was measured using a thermal imager.

Photodegradation of Doxorubicin–Nitrobenezene–Polyethylene Glycol: DOX–NB–PEG was irradiated by UV light for 0, 5, 10, 20, and 40 min, respectively. Then, the chromatogram of these samples and DOX were measured using HPLC. HPLC analysis was performed using a Shimadzu HPLC setup equipped with two LC-8A series pumps coupled to a Shimadzu ELSD-LT II detection system. A linear gradient was carried out over of 10–90% B over 20 min with an initial 5 min hold at 10% B. HPLC buffers: A = H_2O (0.1% trifluoroacetic acid [TFA]); B = Acetonitrile (0.1% TFA).

Chemical Stability: UIDOP micelles were added into various solutions, including serum, medium, and buffers (pH 7.4 and pH 5.0). Then, the absorption spectra were measured during 30 h.

Monitoring of the Singlet Oxygen: The singlet oxygen was detected by a probe called DPBF. The samples with 0.5 µg mL^{-1} of ICG was mixed with DPBF (3 mM), and the solutions were irradiated or not during 600 s; the absorption spectra of the samples were measured at the same time.

Photothermal Effect and Photothermal Conversion Efficiency: To measure the photothermal effect of UIDOP micelles after activation with 980 nm laser, UIDOP micelles at the concentrations of 5, 10, 25, and 50 µg mL^{-1} of ICG were activated with 980 nm laser for 1 min irradiation; then, a thermal imager was used to monitor the temperature elevation of the samples irradiated with 785 nm laser. To evaluate the photothermal conversion efficiency, the activated UIDOP micelles were exposed to the irradiation (785 nm, 1.0 W cm^{-2}) until the temperature no longer rose. Then, the laser was removed so that the temperature of samples was cooling down to room temperature. The temperature was recorded by a digital thermometer during the process.

Cellular Uptake: MNNG/HOS tumor cells (1.0×10^6 cells per well) were seeded on six-well plates. Free ICG, UIDOP micelles, and activated UIDOP micelles (980 nm irradiation, 1 min) were added into the plates for further incubation. The cells were collected and counted at 6 and 24 h-incubation. Subsequently, ICG was extracted from the cells and quantified by Multiskan GO.

Cell Viability: MNNG/HOS cells (5.0×10^3 cells per well) were seeded on 96-well plates. Various groups of samples at different concentration values were added into the plates for 24 h-incubation, followed by the irradiation or without. Then, the cell viability was measured using MTT assay. The CI was calculated by the Equation (1):

$$CI = D(A)/IC_{50}(A) + D(B)/IC_{50}(B) \quad (1)$$

where, D(A) or D(B) represents the IC_{50} of drug A or drug B in the presence of both A and B; IC_{50}(A) or IC_{50}(B) represents the IC_{50} of drug A or drug B alone.

Live–Dead Cell Staining: Live–dead cell staining was performed as previously reported.[41] MNNG/HOS cells (1.0×10^5 cells per well) were seeded on 24-well plates. PBS, UCNP-DOP, and UIDOP micelles were added into the plates, followed by the irradiation at 980 nm for 1 min or without. After 6 h-incubation, the cells were irradiated under 785 nm laser for 3 min or without. After another 1 h, 2 µM of calcein-AM and 8 µM of PI were added into the plates for 30 min-incubation. Then, the cells were washed by PBS for thrice. Finally, the cells were observed and imaged using a fluorescent microscope.

Apoptosis Assay: MNNG/HOS cells (1.0×10^5 cells per well) were seeded on 24-well plates. PBS, UCNP-DOP, and UIDOP micelles were added into the plates for 24 h-incubation, followed by the irradiation with 980 nm laser for 1 min or with 785 nm laser for 3 min. After 24 h,

Annexin V fluorescein isothiocyanate (FITC)/PI were added into the cells for 20 min-incubation at 37 °C. Finally, the apoptosis was measured using flow cytometry.

Disruption of Lysosomal Membranes: MNNG/HOS cells (1.0×10^5 cells per well) were seeded on 24-well plates. UIDOP micelles were added into the plates, followed by the irradiation with 980 nm for 1 min or without. After 6 h-incubation, the cells were irradiated with 785 nm for 3 min or without. After another 1 h, the cells were washed and incubated with acridine orange for 30 min at 37 °C. Finally, the cells were washed and observed using a fluorescent microscope.

Dihydroethidium Staining: MNNG/HOS cells (1.0×10^5 cells per well) were seeded on 24-well plates overnight. The cells were treated with UIDOP micelles and irradiated with 980 nm laser for 1 min or without. After 6 h-incubation, the cells were irradiated with 785 nm for 3 min or without. Subsequently, the cells were washed and incubated with DHE for 30 min at 37 °C. Finally, the cells were washed before subjected to fluorescence microscopical observation.

Intracellular Distribution: MNNG/HOS cells (5.0×10^5 cells per well) were seeded on confocal dishes. UIDOP micelles were added into the dishes and irradiated with 980 nm laser for 1 min or without. After 6 h-incubation, the cells were irradiated with 785 nm laser or not for 3 min. Then, Hoechst 33342 was added into the dishes for 10 min-incubation, followed by 3 min-incubation with LysoTracker Green DND 26. Finally, the cells were washed thrice and observed using a fluorescent microscope.

Cellular Tubulation: BD Matrigel (50 µL per well) was added into 96-well plates on the ice, then the plate was put in the refrigerator at 4 °C for 30 min-incubation, followed by another 30 min-incubation at 37 °C. Subsequently, HUVEC cells (3.0×10^5 cells per well) were mixed with cancer media and UIDOP micelles were added into the plates, followed by the irradiation with 980 nm laser for 1 min and with 785 nm laser for 3 min or without. After 4 h-incubation in Dulbecco's modified eagle medium, containing 1% of fetal bovine serum, the cells were treated with calcein-AM for another 30 min-incubation and observed using a fluorescent microscope. The image was analyzed by image J.

In Vivo Near-Infrared-Fluorescence Imaging and Biodistribution: The experiments were performed in accordance with the Guide for the Care and Use of Laboratory Animals from the Zhejiang Academy of Medical Sciences, and the protocol was approved by the Animal Care and Use Committee of Zhejiang Academy of Medical Sciences. These experiments were approved by the Experimental Animal Ethics Committee of Jiaxing University School of Medicine before the animal experiment operation, and the ethics number is JUMC2019-004. Female Balb/c nude mice bearing MNNG/HOS tumors were created by subcutaneous injection into the flanks of MNNG/HOS cells (5.0×10^6 cells per mouse). Free ICG/DOX, UIDOP micelles were intravenous injected into the mice at the dose of 7.5 mg kg^{-1} of ICG. Then, the tumor was irradiated with 980 nm laser for 1 min at 24 h post-injection. The mice were imaged using IVIS Lumina II at various time points. As for the in vivo biodistribution, the major tissues, including heart, liver, spleen, lung, kidney, and tumor were extracted from the mice at 24 and 72 h post-injection, respectively. Then, these tissues were imaged using IVIS Lumina II.

In Vivo Infrared Thermograph: Free ICG/DOX, UIDOP micelles at the dose of 5.0, 7.5, and 10.0 mg kg^{-1} were intravenously injected into the tumor-bearing mice. Then, the mice injected with UIDOP micelles were irradiated with 980 nm laser for 1 min. After 1 h, all mice were irradiated with 785 nm (1.0 W cm^{-2}) for 5 min. The temperature in tumor region was monitored using a thermal imager.

In Vivo Antitumor Efficiency: The tumor-bearing mice were intravenous injected with PBS, free ICG/DOX, ICG micelles, UCNP-DOP, and UIDOP micelles at the dose of 7.5 mg kg^{-1} of ICG or 1.5 mg kg^{-1} of DOX. Then, the tumors were exposed to the 980 nm irradiation (1.0 W cm^{-2}) for 1 min and 785 nm irradiation (1.0 W cm^{-2}) for 3 min or without at 24 h post-injection. The volume of the tumors was measured using a Vernier caliper during a month. The weight of the mice was also recorded using a weigh. Finally, the tumors were extracted from the mice and photos were taken.

Histological Staining: PBS, ICG micelles, UCNP-DOP, and UIDOP micelles were intravenously injected into the mice bearing MNNG/HOS tumor. Then, the tumors were irradiated with the 980 or 785 nm laser. 6 h later, the major tissues, including heart, liver, spleen, lung, kidney, and tumor were extracted from the mice and immersed into 4% of formaldehyde solution for 24 h. Next, the tissues were cut into slice and exposed to H&E staining.[42] Finally, the organ slices were observed and imaged by a microscope. As for the Ki-67, the authors determined the tumors between this group. The tumor was cut into slices and incubated with blocking fluid for 20 min, followed by the incubation with Ki-67 overnight at 4 °C. Next, the organ slices were washed and incubated with the secondary antibody. Finally, the slices were observed using a microscope.

Statistical Analysis: The normalization of the data was performed by comparison with PBS group or the sample at 0 h. The data were reported as mean ± SD. Sample size (n) for each statistical analysis was shown in figure legend. The data were analyzed by paired t-test using GraphPad Prism software.

Supporting Information

Supporting Information is available from the Wiley Online Library or from the author.

Acknowledgements

H.L., L.K., and F.Z. contributed equally to this work. Financial supports from the Zhejiang Provincial Medicine and Health Technology Project (2020RC125), National Key Research and Development Program of China (2020YFA0908200), National Natural Science Foundation of China (81930051 and 81871472), Jiaxing Public Welfare Research Program (2020AY30021), HiLIFE Research Funds, the Sigrid Jusélius Foundation, and the Academy of Finland (Grant No. 317042) are acknowledged.

Conflict of Interest

The authors declare no conflict of interest.

Data Availability Statement

Research data are not shared.

Keywords

light-controlled nanosystems, size-flexibility, tumor ablation, up-conversion nanoparticles

Received: February 19, 2021
Revised: March 4, 2021
Published online:

[1] P. Couvreur, *Adv. Drug Delivery Rev.* **2013**, *65*, 21.
[2] J. K. Patra, G. Das, L. F. Fraceto, E. V. R. Campos, M. d. P. Rodriguez-Torres, L. S. Acosta-Torres, L. A. Diaz-Torres, R. Grillo, M. K. Swamy, S. Sharma, S. Habtemariam, H.-S. Shin, *J. Nanobiotechnol.* **2018**, *16*, 71.
[3] J. Shi, P. W. Kantoff, R. Wooster, O. C. Farokhzad, *Nat. Rev. Cancer* **2017**, *17*, 20.
[4] V. P. Chauhan, R. K. Jain, *Nat. Mater.* **2013**, *12*, 958.
[5] T. Lammers, F. Kiessling, W. E. Hennink, G. Storm, *J. Controlled Release* **2012**, *161*, 175.

[6] S. Chen, C. Xing, D. Huang, C. Zhou, B. Ding, Z. Guo, Z. Peng, D. Wang, X. Zhu, S. Liu, Z. Cai, J. Wu, J. Zhao, Z. Wu, Y. Zhang, C. Wei, Q. Yan, H. Wang, D. Fan, L. Liu, H. Zhang, Y. Cao, *Sci. Adv.* **2020**, *6*, eaay6825.
[7] M. J. Ernsting, M. Murakami, A. Roy, S.-D. Li, *J. Controlled Release* **2013**, *172*, 782.
[8] W. Yu, R. Liu, Y. Zhou, H. Gao, *ACS Cent. Sci.* **2020**, *6*, 100.
[9] H. Kang, S. Rho, W. R. Stiles, S. Hu, Y. Baek, D. W. Hwang, S. Kashiwagi, M. S. Kim, H. S. Choi, *Adv. Healthcare Mater.* **2020**, *9*, 1901223.
[10] S. Mura, J. Nicolas, P. Couvreur, *Nat. Mater.* **2013**, *12*, 991.
[11] L. L. Tayo, *Biophys. Rev.* **2017**, *9*, 931.
[12] P. Mi, *Theranostics* **2020**, *10*, 4557.
[13] M. Qiu, D. Wang, W. Liang, L. Liu, Y. Zhang, X. Chen, D. Sang, C. Xing, Z. Li, B. Dong, F. Xing, D. Fan, S. Bao, H. Zhang, Y. Cao, *Proc. Natl. Acad. Sci. USA* **2018**, *115*, 501.
[14] M. A. C. Stuart, W. T. S. Huck, J. Genzer, M. Müller, C. Ober, M. Stamm, G. B. Sukhorukov, I. Szleifer, V. V. Tsukruk, M. Urban, F. Winnik, S. Zauscher, I. Luzinov, S. Minko, *Nat. Mater.* **2010**, *9*, 101.
[15] L. Yu, H. Ke, F. S. Du, Z. Li, *Biomacromolecules* **2019**, *20*, 2809.
[16] Y. Wang, Y. Deng, H. Luo, A. Zhu, H. Ke, H. Yang, H. Chen, *ACS Nano* **2017**, *11*, 12134.
[17] L. Yu, H.-L. Ke, F.-S. Du, Z.-C. Li, *Biomacromolecules* **2019**, *20*, 2809.
[18] C. Wang, J. Wang, X. Zhang, S. Yu, D. Wen, Q. Hu, Y. Ye, H. Bomba, X. Hu, Z. Liu, *Sci. Transl. Med.* **2018**, *10*, eaan3682.
[19] X. An, A. Zhu, H. Luo, H. Ke, H. Chen, Y. Zhao, *ACS Nano* **2016**, *10*, 5947.
[20] J. F. Quinn, M. R. Whittaker, T. P. Davis, *Polym. Chem.* **2017**, *8*, 97.
[21] J. Kalia, R. T. Raines, *Angew. Chem., Int. Ed.* **2008**, *47*, 7523.
[22] B. Liu, S. Thayumanavan, *J. Am. Chem. Soc.* **2017**, *139*, 2306.
[23] X. Ma, N. Zhou, T. Zhang, Z. Guo, W. Hu, C. Zhu, D. Ma, N. Gu, *RSC Adv.* **2016**, *6*, 13129.
[24] J. Lee, K. H. Ku, J. Kim, Y. J. Lee, S. G. Jang, B. J. Kim, *J. Am. Chem. Soc.* **2019**, *141*, 15348.
[25] A. Díaz-Moscoso, P. Ballester, *Chem. Commun.* **2017**, *53*, 4635.
[26] T. Yan, F. Li, S. Qi, J. Tian, R. Tian, J. Hou, Q. Luo, Z. Dong, J. Xu, J. Liu, *Chem. Commun.* **2020**, *56*, 149.
[27] A. A. Beharry, G. A. Woolley, *Chem. Soc. Rev.* **2011**, *40*, 4422.
[28] J. W. Rabalais, *J. Chem. Phys.* **1972**, *57*, 960.
[29] L. Kortekaas, W. R. Browne, *Chem. Soc. Rev.* **2019**, *48*, 3406.
[30] S. He, H. Li, H. Chen, *J. Mater. Sci.* **2018**, *53*, 14337.
[31] S. Wen, J. Zhou, K. Zheng, A. Bednarkiewicz, X. Liu, D. Jin, *Nat. Commun.* **2018**, *9*, 2415.
[32] M. Wang, G. Abbineni, A. Clevenger, C. Mao, S. Xu, *Nanomedicine* **2011**, *7*, 710.
[33] A. R. Rastinehad, H. Anastos, E. Wajswol, J. S. Winoker, N. J. Halas, *Proc. Natl. Acad. Sci. USA* **2019**, *116*, 18590.
[34] D. Jaque, L. M. Maestro, B. del Rosal, P. Haro-Gonzalez, A. Benayas, J. L. Plaza, E. M. Rodríguez, J. G. Solé, *Nanoscale* **2014**, *6*, 9494.
[35] J. Hu, H. Luo, Q. Qu, X. Liao, C. Huang, J. Chen, Z. Cai, Y. Bao, G. Chen, B. Li, W. Cui, *ACS Appl. Mater. Interfaces* **2020**, *12*, 42511.
[36] H. Luo, Q. Wang, Y. Deng, T. Yang, H. Ke, H. Yang, H. He, Z. Guo, D. Yu, H. Wu, H. Chen, *Adv. Funct. Mater.* **2017**, *27*, 1702834.
[37] Z. Guo, H. He, Y. Zhang, J. Rao, T. Yang, T. Li, L. Wang, M. Shi, M. Wang, S. Qiu, X. Song, H. Ke, H. Chen, *Adv. Mater.* **2020**, *33*, 2004225.
[38] Q. Liu, Z. Xie, M. Qiu, I. Shim, Y. Yang, S. Xie, Q. Yang, D. Wang, S. Chen, T. Fan, B. Ding, Z. Guo, D. Adah, X. Yao, Y. Zhang, H. Wu, Z. Wu, C. Wei, H. Wang, H. Kim, Q. Zou, Q. Yan, Z. Cai, J. Kim, L. Liu, H. Zhang, Y. Cao, *Adv. Sci.* **2020**, *7*, 2001191.
[39] D. R. Kearns, P. B. Merkel, *J. Am. Chem. Soc.* **1972**, *94*, 7244.
[40] L. Cheng, Z. Cai, T. Ye, X. Yu, Z. Chen, Y. Yan, J. Qi, L. Wang, Z. Liu, W. Cui, L. Deng, *Adv. Funct. Mater.* **2020**, *30*, 2001196.
[41] X. He, X. Yin, J. Wu, S. Wickström, Y. Duo, Q. Du, S. Qin, S. Yao, X. Jing, K. Hosaka, J. Wu, L. Jensen, A. Lundqvist, A. Salter, L. Bräutigam, W. Tao, Y. Chen, R. Kiessling, Y. Cao, *Proc. Natl. Acad. Sci. USA* **2020**, *117*, 22910.
[42] X. Sun, X. He, Y. Zhang, K. Hosaka, P. Andersson, J. Wu, J. Wu, X. Jing, Q. Du, X. Hui, B. Ding, Z. Guo, A. Hong, X. Liu, Y. Wang, Q. Ji, R. Beyaert, Y. Yang, Q. Li, Y. Cao, *Gut* **2021**, *0*, 1.